Research in Astronomy and Astrophysics, 23:065010 (18pp), 2023 June https://doi.org/10.1088/1674-4527/accbb2

Detection of TiO and VO in the Atmosphere of WASP-121b and Evidence For its Temporal Variation

Qinglin Ouyang[1,2], Wei Wang[3], Meng Zhai[1], Guo Chen[4], Patricio Rojo[5], Yujuan Liu[3], Fei Zhao[3], Jia-Sheng Huang[1], and Gang Zhao[2,3]

[1] Chinese Academy of Sciences South America Center for Astronomy (CASSACA), National Astronomical Observatories, Beijing 100101, China; mzhai@nao.cas.cn
[2] School of Astronomy and Space Science, University of Chinese Academy of Sciences (UCAS), Beijing 100049, China
[3] CAS Key Laboratory of Optical Astronomy, National Astronomical Observatories, Chinese Academy of Sciences, Beijing 100101, China; wangw@nao.cas.cn
[4] CAS Key Laboratory of Planetary Sciences, Purple Mountain Observatory, Chinese Academy of Sciences, Nanjing 210023, China
[5] Departamento de Astronomía, Universidad de Chile, Camino El Observatorio 1515, Las Condes, Santiago, Chile
Received 2023 January 30; revised 2023 March 22; accepted 2023 March 27; published 2023 May 17

Abstract

We report the transit observations of the ultra-hot Jupiter WASP-121b using the Goodman High Throughput Spectrograph at the 4 m ground-based Southern Astrophysical Research Telescope, covering the wavelength range 502–900 nm. By dividing the target and reference star into 19 spectroscopic passbands and applying differential spectrophotometry, we derive spectroscopic transit light curves and fit them using a Gaussian process framework to determine transit depths for every passband. The obtained optical transmission spectrum shows a steep increased slope toward the blue wavelength, which seems to be too steep to be accounted for by Rayleigh scattering alone. We note that the transmission spectrum from this work and other works differ obviously from each other, which was pointed out previously by Wilson et al. as evidence for temporal atmospheric variation. We perform a free chemistry retrieval analysis on the optical transmission spectra from this work and the literature HST/WFC3 NIR spectrum. We determine TiO, VO and H_2O with abundances of $-5.95^{+0.47}_{-0.42}$ dex, $-6.72^{+0.51}_{-1.79}$ dex and $-4.13^{+0.63}_{-0.46}$ dex, respectively. We compare the abundances of all three of these molecules derived from this work and previous works, and find that they are not consistent with each other, indicating the chemical compositions of the terminator region may change over long timescales. Future multi-epoch and high-precision transit observations are required to further confirm this phenomenon. We note that when combining the transmission spectra in the optical and in NIR in retrieval analysis, the abundances of V and VO, the NIR-to-optical offset and the cloud deck pressure may be coupled with each other.

Key words: methods: data analysis – techniques: spectroscopic – stars: individual (WASP-121) – Planetary Systems – planets and satellites: atmospheres

1. Introduction

Transmission spectroscopy is by far the most important technique in the study of exoplanet atmospheres. By determining the transit depths at different wavelengths (Charbonneau et al. 2000; Deming et al. 2013; Madhusudhan 2019), one can measure the absorption features of the planetary atmosphere and set constraints on the physical structure and chemical composition of the atmosphere at the day-night terminator region. Until now, many molecules and atoms, such as H_2O, CH_4, CO_2, TiO, VO, Na, K and Fe (Beaulieu et al. 2010; Casasayas-Barris et al. 2017; Sedaghati et al. 2017; Chen et al. 2018; Ehrenreich et al. 2020; Giacobbe et al. 2021), have been discovered in exoplanet atmospheres by transmission spectroscopy using large ground-based telescopes or space telescopes.

Ultra-hot Jupiters (UHJs) are a class of hot Jupiter-like planets with high temperatures ($\geqslant$2000 K) and small distances to their host stars. They are excellent targets for transmission spectroscopy, and ideal laboratories for studying extreme chemistry and climates of exoplanets (Lothringer et al. 2018). Such extremely high temperatures can make some refractory metals exist solely in their atomic states rather than molecular states (Hoeijmakers et al. 2018), while the very close host star may photoionize some atoms in the upper atmosphere (Deibert et al. 2021). On the other hand, a UHJ with atmospheric circulation makes some atoms evaporate on the day side and condense on the night side, such as "iron rain" in the atmosphere of WASP-76 b, discovered by Ehrenreich et al. (2020). Moreover, thermal inversion is frequently found on UHJs, due to the extra heating of the upper atmospheres by metal species (Lothringer et al. 2018; Gandhi et al. 2020).

WASP-121b is an inflated UHJ discovered by Delrez et al. (2016) with $M_p = 1.183\,M_{Jup}$ and $R_p = 1.865\,R_{Jup}$. Due to the high irradiation and short period ($T_{eq} \geqslant 2400$ K, $P = 1.275$ days), it is one of the most well-studied UHJs using low-

resolution (LR) transmission spectroscopy and high-resolution (HR) Doppler spectroscopy. Evans et al. (2016) first reported the H_2O detection and tentative TiO or VO absorptions from the near-infrared (NIR) transmission spectrum using the Hubble Space Telescope (HST). The following HST secondary eclipse observation confirmed the detection of H_2O, and revealed the thermal inversion in the atmosphere of WASP-121b, making it the first exoplanet found to contain a stratosphere (Evans et al. 2017). However, none of the two subsequent secondary eclipse studies (Mikal-Evans et al. 2019, 2020) confirmed the existence of TiO and VO. The very recent spectroscopic phase curve observation of WASP-121b by Mikal-Evans et al. (2022) found that the temperature profile had changed from getting warmer with altitude on the dayside hemisphere to turning cooler with altitude on the nightside hemisphere. This effect may be significant enough to cause the condensation of metal oxides on the nightside, which may explain the nondetection of TiO and VO. Using HR Doppler spectroscopy, an atomic library in the WASP-121b atmosphere was discovered by different instruments. Gibson et al. (2020) and Cabot et al. (2020) both detected Fe using the UVES and High Accuracy Radial Velocity Planet Searcher (HARPS) spectrographs, respectively. Then the atoms Cr and V were found by Ben-Yami et al. (2020) using archival HARPS data. These two atoms were then confirmed by Hoeijmakers et al. (2020), who detected several new species including Mg, Na, Ca and Ni. On the other hand, the hydrodynamic simulation of Hα developed by Yan et al. (2021) suggested an expanding hydrogen envelope around this planet. The transmission spectrum obtained by Gemini/GMOS supported the possibility of temporal variation of the atmosphere of this particular planet (Wilson et al. 2021). Recently, several HR abundance retrieval studies were performed successfully for this planet, including, e.g., Gibson et al. (2022) and Maguire et al. (2023), who reported consistent relative abundance measurements of Fe, Cr and V based on the data from UVES and ESPRESSO, respectively.

Here we present the optical transmission spectrum of WASP-121b, obtained by the Goodman High Throughput Spectrograph (GHTS, Clemens et al. 2004) installed on the 4.1 m Southern Astrophysical Research Telescope (SOAR), in Cerro Pachón, Chile. Recently, transmission spectrophotometry studies with 4 m class telescopes became a new option in addition to ground-based 6–10 m telescopes or space telescopes, including the Low Resolution Ground-Based Exoplanet Survey using Transmission Spectroscopy (LRG-BEAST, Kirk et al. 2016, 2017, 2018, 2019, 2021; Alderson et al. 2020) and our recent work (Ouyang et al. 2023).

In this work, we aim to investigate the presence of TiO/VO molecules or high-altitude clouds and hazes, which may provide us an opportunity to better understand the stratosphere of WASP-121b. This manuscript is organized as follows. We first introduce the observation and data reduction in Section 2, and then present the light curve analysis in Section 3. In Section 4 we describe our retrieval analysis, followed by the discussion and conclusion in Sections 5 and 6, respectively.

2. Observation and Data Reduction

2.1. Observation

The observations of WASP-121b were taken on the nights of 2018 February 7 (hereafter Night 1) and 2018 March 1 (hereafter Night 2), using GHTS installed on SOAR (Program CN2018A-89, PI: Wei Wang). In order to monitor and correct the telluric variation, the Multi-Object Spectroscopy (MOS) mode of GHTS was used to simultaneously observe the target WASP-121 and the reference star HD 55273 for differential spectrophotometry. The target and reference stars have similar V magnitudes (10.51 versus 10.10; Høg et al. 2000) and an angular separation of $\sim$166.″92.

The slit mask we used contains two pre-carved long wide slits, with one for the target star and the other for the reference star. The slits were set to have a projected width of 20″, to avoid slit loss that may occur in case of large seeing variation. The 400 M2 grating was used, which provides wavelength coverage 500–905 nm and spectral resolution $R \sim 1850$ with a seeing size of $\sim$0.″45. We employed the GG455 filter, to block the second-order contamination, and the 2×2 binning mode (0.″30 per binned pixel) for detector readout.

The two transit observations cover the UT window of 01:57–03:20 from Night 1 and 00:53–06:06 from Night 2, respectively. However, due to the dewpoint alert, at UT 03:21, the observation of Night 1 stopped about 1 hr before the predicted mid-transit time, $T_{\rm mid} = 04{:}39$. During Night 2, there was a small gap starting from roughly 80 minutes after the transit center. This is because the target and reference stars were slightly offset from the slit center and it took a few minutes to redo the acquisition. In total, we obtained 69 and 213 exposures for each night, with exposure times of 40–100 s. The details on both observations are shown in Table 1. As only the Night 2 transit was covered entirely, the following data reduction procedure was only applied to the Night 2 data.

2.2. Data Reduction

The raw data set of Night 2 was reduced using `IRAF` (Tody 1986, 1993), with the associated Python scripts written by us. We first corrected the overscan, bias and flat field for the 2D spectra, and used the `dcr` package (Pych 2004) to remove cosmic ray hits. The 1D spectral extraction procedure was done by the optimal extraction algorithm developed by Horne (1986). To minimize the point-to-point scatter in the light curves, we also tested a series of aperture widths from 17 to 35 pixels. The aperture width of 32 pixels was finally chosen, which yielded the smallest out-of-transit scatter. For the wavelength calibration, the initial wavelength solution was

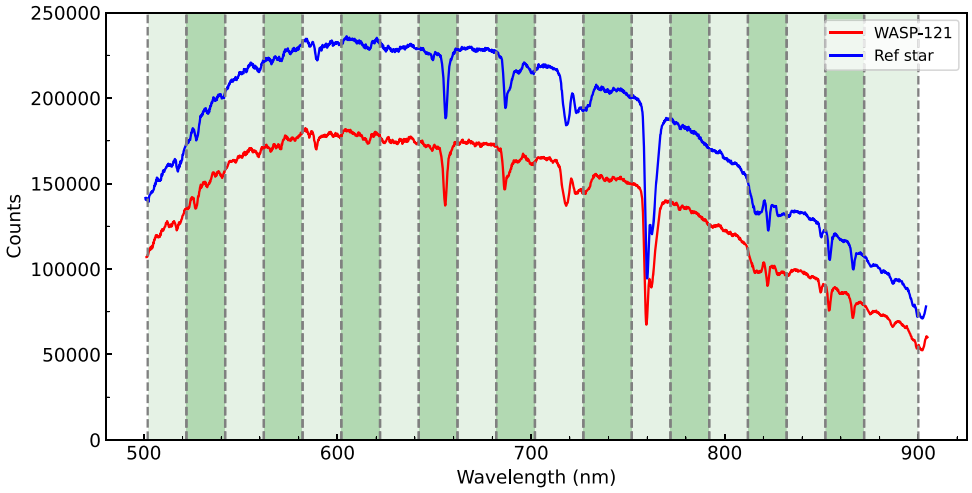

Figure 1. Example spectra of WASP-121 (red) and reference star (blue) for Night 2. The dark and light green shaded zones indicate the individual passbands used in this work.

Table 1
Details of the Two Transit Observations

Observation Night	Instrument	Start time (UTC)	End Time (UTC)	Exposure Time (s)	Exposure Number	Airmass Range
2018-2-7[a]	SOAR/GHTS	01:57:22	03:21:34	40−60	69	1.03−1.01−1.02
2018-3-1	SOAR/GHTS	00:53:59	06:06:52	60−100	213	1.02−1.01−1.95

Note.
[a] The data taken on 2018 February 7 are not used for the following data analysis.

derived using `identify` in `IRAF` from the HgArNe arc lamp spectra taken before and after science frames. Then the wavelength solution was refined by aligning all 1D spectra in the wavelength domain, using the strong telluric lines such as telluric O_2. The timestamp of each spectrum was set as the mid-exposure time, which is converted into Barycentric Julian Dates in Barycentric Dynamical Time (BJD_{TDB}; Eastman et al. 2010).

The white transit light curve was derived by differential spectrophotometry. We first integrated the fluxes within the wavelength range from 502 to 900 nm for both the target and reference star, and then divided the target starlight curve by the reference starlight curve, in order to remove the telluric and instrumental effects. The spectroscopic transit light curves were created by a similar process for each of the pre-divided spectral channels. Following our experience in Ouyang et al. (2023), we used 19 channels with 16 channels having widths of 20 nm, 2 channels of 25 nm (702−727 nm and 727−752 nm) and 1 of 28 nm (872−900 nm). Such division is to prevent the edge of each channel from falling on the prominent stellar absorption lines. Figure 1 displays example spectra of the target and reference star of Night 2, along with the 19 spectral channels shown in the shaded light and dark green. The raw light curves of Night 2 for the target and reference star are featured in Figure 2 in red and blue, respectively.

3. Light Curve Analysis

3.1. White Light Curve Analysis

The white light curve of Night 2 was generated by summing the flux between 502 and 900 nm. The derived light curves are considered to include two independent components, one component is the astrophysical transit signals and the other is noise. The former could be modeled by an analytic transit model (e.g., the MA02 Model; Mandel & Agol 2002) and noise, including the Gaussian noise (e.g., shot noise) and correlated systematics induced by telluric or instrumental effects during the observation. Therefore, we treated the light curves as a Gaussian process (GP, Rasmussen & Williams 2006) with the MA02 model to find the systematics and transit depths. The GP method was first adopted in transit light curve analysis in Gibson et al. (2012), and then widely used in the study of transmission spectroscopy of exoplanets (Gibson et al. 2013; Evans et al. 2015, 2017; Chen et al. 2021b) and our recent work by Ouyang et al. (2023). It has the advantage of finding internal correlations between various parameters

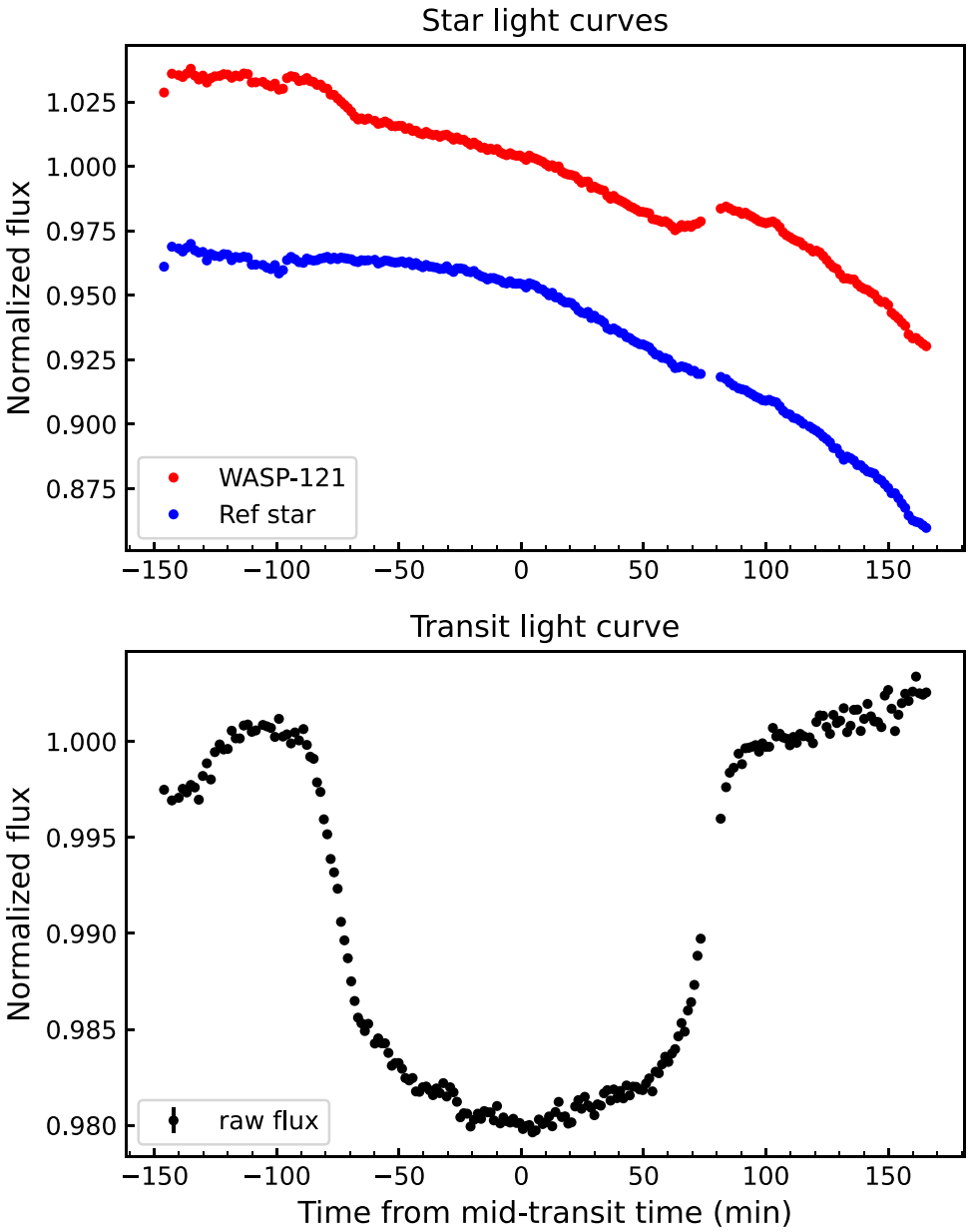

Figure 2. The normalized white light curves of Night 2. Top: raw stellar light curves of WASP-121 (red) and reference star (blue) with the latter vertically shifted for clarity. Both light curves are normalized by the median value of out-of-transit flux. Bottom: the target-to-reference differential light curve normalized by the median value of out-of-transit flux.

without providing specific functions and assessing how reliable these correlations are. In this section, we apply the GP method to analyze our light curves. The details are described in the following.

We treated the white light curve as a GP:

$$f(\boldsymbol{t}, \boldsymbol{x}) \sim \mathcal{GP}(T(\boldsymbol{t}, \phi), \boldsymbol{\Sigma}(\boldsymbol{x}, \boldsymbol{\theta})), \quad (1)$$

where $T(\boldsymbol{t}, \phi)$ is the transit function described by time series $\boldsymbol{t}$ and transit parameters ϕ. $\boldsymbol{\Sigma}$ is the covariance matrix, which is a function of additional parameters $\boldsymbol{x}$ and hyperparameters $\boldsymbol{\theta}$ of GP. Additional parameters such as airmass, seeing, and spectral trace movement in both the spectral and spatial directions vary with time during the observation, which may induce systematics. Correlations between data points are described using the covariance matrix, the elements of which are given by

$$\boldsymbol{\Sigma}(x_{\rm n}, x_{\rm m}) = k(x_{\rm n}, x_{\rm m}), \quad (2)$$

where k is the kernel function (or covariance function), which decides each element in the covariance matrix from additional parameters. In our case, we chose the Matérn $\nu = 3/2$ kernel

Table 2
The BIC Values Calculated using the GP Likelihood of Different Parameter Combinations as GP Inputs

GP Inputs	BIC	ΔBIC
time, airmass, seeing, x, y	−2798.96	22.08
time, seeing, x, y	−2806.71	14.33
time, seeing, x	−2809.40	11.64
time, seeing, y	−2812.76	8.28
time, x, y	−2811.77	9.27
time, seeing	−2815.48	5.56
time	**−2821.04**	**0**

Note. The best parameter combination is shown in bold.

which is widely employed in transit light curve analysis (Gibson et al. 2013; Chen et al. 2021a, 2021b). The kernel is defined as

$$k(x_{\rm n}, x_{\rm m}) = A(1 + \sqrt{3}R_{\rm nm})e^{-\sqrt{3}R_{\rm nm}}, \quad (3)$$

where A and R are the hyperparameters specifying the amplitude and scale of the kernel, respectively.

We implemented GP via the Python package `george` (Ambikasaran et al. 2015), where the mean function of GP is the MA02 model implemented via the Python package `batman` (Kreidberg 2015). We assumed a circular orbit with a fixed period derived by Delrez et al. (2016). As for the additional parameters, we explored all the combinations of the parameters, e.g., time, airmass, seeing, and the position of the target star in the spatial (x) and dispersion (y) directions, and then we chose the best parameter combination with the smallest Bayesian Information Criterion (BIC, Schwarz 1978). As shown in Table 2, it turns out that employing time alone as the correlating parameter returns the minimal BIC and is therefore adopted in this work.

To account for the stellar limb darkening (LD) effect on the transit light curve, the quadratic LD law was adopted and the coefficients u_1 and u_2 were fitted using Gaussian priors. The priors were calculated by the Python package `PyLDTk` (Parviainen & Aigrain 2015), which utilizes the library of PHOENIX-generated specific intensity spectra by Husser et al. (2013). The stellar parameters reported by the discovery paper Delrez et al. (2016) were used, with the stellar effective temperature $T_{\rm eff} = 6460 \pm 140$ K, surface gravity $\log g_\star = 4.2 \pm 0.2$ and metallicity $Z = 0.13 \pm 0.09$.

Then the Affine Invariant Markov Chain Monte Carlo (MCMC) was utilized via the Python package `emcee` (Foreman-Mackey et al. 2013) to explore the marginalized posterior distributions of all fitting parameters. They are the mid-transit time $T_{\rm mid}$, the planet-to-star radius ratio $R_{\rm p}/R_\star$, the scaled semimajor axis $a/R_\star$, the orbit inclination i, LD coefficients u_1 and u_2, the hyperparameters of kernel function (A and R) and the white noise jitter term $\sigma_{\rm w}$ which is to account for additional light curve uncertainties. The period P and eccentricity e were fixed to the values listed in Delrez et al. (2016). Our MCMC procedure consisted of 100 walkers, each one with 20,000 steps, and the first 4000 steps were set as the "burn-in" phase. The chain length is kept to be more than 50 times the autocorrelation time to ensure convergence. The white light curve and the best-fit model are shown in Figure 3. The priors and posterior distributions of the fitting parameters are listed in Table 3.

3.2. Spectroscopic Light Curves Analysis

The "raw" spectroscopic light curves were created by summing the flux in every channel described in Section 2. They were divided by common-mode noise before GP fitting. This method is called "divide-white". The divide-white method is widely used in transmission spectroscopy. Common-mode noise is created by dividing the white light curve with its best-fit transit model. Next, the light curve in each channel was modeled separately to derive the wavelength-dependent parameters, which are $R_{\rm p}/R_\star$, u_1 and u_2. The wavelength-independent parameters ($T_{\rm mid}$, $a/R_\star$, i) with the best-fit values are derived from the white light curve fitting (Table 3). The number of MCMC walkers was set to be 50 and each walker contained 20,000 steps, with the first 4000 steps being the "burn-in" phase. All the 19 spectroscopic light curves with their best-fit models are featured in Figure 4.

4. Transmission Spectrum

4.1. The Transmission Spectra

The derived $R_{\rm p}/R_\star$ of all the 19 passbands are listed in Table 4, and the corresponding transmission spectrum is depicted in Figure 5. As described in Section 1, the transmission spectra of this planet have been obtained by several previous works, using different ground-based and space-based instruments (Delrez et al. 2016; Evans et al. 2016, 2018; Wilson et al. 2021, or D16, E16, E18 and W21 for short, respectively). It is well worth comparing our obtained SOAR optical spectrum (hereafter the OPT data) with them for a consistency check and to explore evidence of temporal changes in exoplanetary atmospheres.

We show in Figure 6 the transmission spectra from the OPT data and from D16, E16, E18 and W21. It is obvious from the plot that OPT (the black open circles) shows a large discrepancy from the others, with a relatively larger effective planet radius and steeper slope toward blue. The discrepancy may be caused by slightly different input parameters such as $a/R_\star$ and i. Note that W21 employed the orbital parameters the same as the reported value in E18 (i.e., $a/R_\star = 3.86$, $b = 0.06$) and using a Gaussian prior centered on the E18 value for $R_{\rm p}/R_\star$, i.e., $\mathcal{N}(0.1219, 0.0005)$, which are different from ours as listed in Table 3. It is pointed out by Alexoudi et al. (2018) and Alexoudi et al. (2020) that employing different input

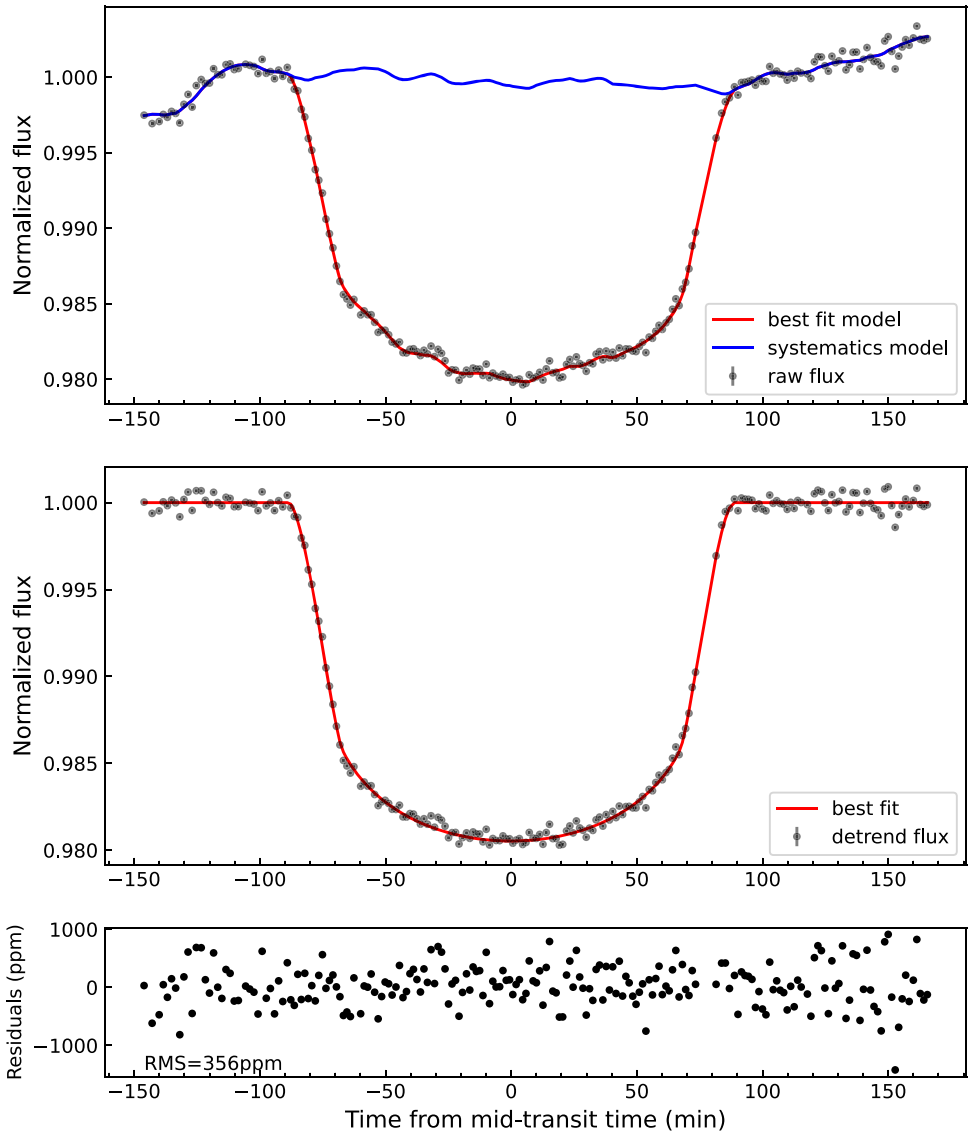

Figure 3. The raw, detrended light curves and residuals for Night 2 are displayed from top to bottom successively. The black dots, and red and blue lines represent the data, the best fit models, and the systematic model, respectively. The bottom panel shows the residuals obtained by subtracting the best fit model from the data, with an rms of 356 ppm.

orbital parameters may induce notable discrepancies in transmission spectra, which are likely to be a steeper slope for the cases of K- and F- type stars or a feature at blue wavelengths for M-type stars. The difference between the SOAR and W21 Gemini transmission spectra, i.e., $\Delta R_{\rm p}^2/R_\star^2$, is ∼1453 ppm. However, the discrepancy still remains, albeit a bit smaller, with $\Delta R_{\rm p}^2/R_\star^2 \sim 1216$ ppm, when we use the orbital parameters exactly the same as in W21 to redo the SOAR white light curve fitting. Only if a stringent Gaussian prior like the W21 one is adopted can the offset become close to zero. Even in such a case, the shape of the newly derived SOAR transmission spectrum remains obviously different from the W21 spectrum, as affirmed by the filled circles in Figure 6. We thus conclude that using different orbital parameters should not be the major cause for the observed discrepancy between the three optical transmission spectra in WASP-121b's case.

There is a possibility that the data analysis processes used in this work lead to biased results. To examine this possibility, we performed a new data analysis on the two-night Gemini/GMOS 1D spectra provided by the authors of W21 via private communication and derived a "new" GMOS transmission spectrum. The white and spectroscopic light curves were created mainly following the procedures described in Section 2 of W21 using our pipeline. For the light curve analysis, we followed the same procedure described in Section 3. We treated

Table 3
The Priors and Posterior Results For the White Light Curve Analysis

Parameter	Prior	Posterior
Period (days)	1.2749255[a]	⋯
e	0[a]	⋯
$T_{\rm mid}$ [MJD][b]	$\mathcal{U}$(8179.60, 8179.70)	$8179.64181^{+0.00028}_{-0.00027}$
$R_{\rm p}/R_\star$	$\mathcal{U}$(0.10, 0.20)	$0.12772^{+0.00229}_{-0.00322}$
$a/R_\star$	$\mathcal{U}$(0, 5)	$3.74^{+0.03}_{-0.03}$
i(deg)	$\mathcal{N}$(87.6, 0.6)	$87.28^{+0.60}_{-0.58}$
u_1	$\mathcal{N}$(0.439, 0.006)	$0.43950^{+0.00544}_{-0.00543}$
u_2	$\mathcal{N}$(0.139, 0.008)	$0.13917^{+0.00853}_{-0.00864}$
ln A	$\mathcal{U}(-20, -1)$	$-12.96^{+0.84}_{-0.60}$
ln R_t	$\mathcal{U}(-15, 15)$	$-7.23^{+0.82}_{-0.68}$
ln $\sigma_{\rm w}$	$\mathcal{U}(-20, -1)$	$-15.89^{+0.12}_{-0.12}$

Notes.
[a] These parameters were fixed in light curve modeling, expressed in Modified Julian Date (MJD), using the values from Delrez et al. (2016).
[b] MJD = $\rm BJD_{TDB}$—2450000.

Table 4
The Planet-to-star Radius Ratios of All Passbands from Night 2

Wavelength Center (nm)	Width (nm)	$R_{\rm p}/R_\star$
512.0	20	$0.13058^{+0.00100}_{-0.00097}$
532.0	20	$0.12601^{+0.00375}_{-0.00293}$
552.0	20	$0.13031^{+0.00228}_{-0.00203}$
572.0	20	$0.13079^{+0.00236}_{-0.00211}$
592.0	20	$0.13096^{+0.00140}_{-0.00189}$
612.0	20	$0.13060^{+0.00097}_{-0.00120}$
632.0	20	$0.13079^{+0.00065}_{-0.00089}$
652.0	20	$0.12738^{+0.00058}_{-0.00059}$
672.0	20	$0.12879^{+0.00093}_{-0.00089}$
692.0	20	$0.12599^{+0.00113}_{-0.00075}$
714.5	25	$0.12665^{+0.00076}_{-0.00113}$
739.5	25	$0.12604^{+0.00119}_{-0.00121}$
762.0	20	$0.12445^{+0.00168}_{-0.00170}$
782.0	20	$0.12467^{+0.00143}_{-0.00145}$
802.0	20	$0.12328^{+0.00173}_{-0.00183}$
822.0	20	$0.12481^{+0.00174}_{-0.00192}$
842.0	20	$0.12346^{+0.00267}_{-0.00287}$
862.0	20	$0.12610^{+0.00222}_{-0.00234}$
886.0	28	$0.12496^{+0.00274}_{-0.00296}$

the priors of all fitting parameters the same as done in W21 and fitted two-night data jointly using our Python scripts. The new transmission spectrum we obtained from the GMOS data is consistent with the published one in W21 (Figure A1), with a small offset, $\sim 472 \pm 286 \pm 25$ ppm.

The small offset between the two spectra is not surprising because our data analysis process is not exactly the same as that in W21. For example, in the white light curve analysis, they fixed orbital parameters to the value from E18, i.e., $a/R_\star = 3.86$, $b = 0.06$, and set an extremely small Gaussian prior to $R_{\rm p}/R_\star$, i.e., $\mathcal{N}(0.1219, 0.0005)$. In our case, we fix $a/R_\star = 3.86$, inclination $i = 89.^\circ1$ and $R_{\rm p}/R_\star \sim \mathcal{U}(0.1, 0.2)$. The value of i is set to correspond to $b = 0.06$ at the given $a/R_\star$. So, the only difference in parameter setting is the prior of $R_{\rm p}/R_\star$ - W21 used a narrow Gaussian distribution so that $R_{\rm p}/R_\star$ could hardly be changed, while we adopted a much looser uniform distribution.

More importantly, these two spectra share the same overall trend and distribution, as indicated by the linear fittings and the Kolmogorov–Smirnov (K-S) test. The linear fittings are performed between the obtained transit depths and the wavelength in nanometers of the two transmission spectra, which yield quite similar linear coefficients (-1.92×10^{-6} of "new" GMOS versus -1.99×10^{-6} of W21), and the K-S test implies that these two data points probably originate from the same probability distribution at a confidence level of 95% with a quite small D statistic of 0.094. Therefore, we conclude that the data analysis procedures employed in this work do not lead to any significant bias or trend, and the observed discrepancies between this work and all the others are likely to be real, i.e., there may be temporal changes in the atmosphere. This is supported by the fact that all the other three transmission spectra are different from each other as well, having both different mean values and slopes.

4.2. The Steep Slope in the Transmission Spectrum

The steep increased slope toward the blue wavelength is shown in Figure 5, which we first consider as the result of Rayleigh scattering in the atmosphere of WASP-121b. Lecavelier Des Etangs et al. (2008) pointed out that the measured effective planet radius related to Rayleigh scattering should be a function of the wavelength, which is given by

$$\frac{dR_p}{d\ \ln \lambda} = \alpha H = \alpha \frac{k_B T}{\mu g}, \tag{4}$$

where H is the scale height of the planet's atmosphere, T is the planetary temperature, $k_{\rm B}$ is the Boltzmann constant, μ is the mean mass of atmospheric particles and g is the gravity of the planet. According to the derivation in Section 3 of Lecavelier Des Etangs et al. (2008), the value of α caused by Rayleigh scattering should be close to -4.

We fit the transmission spectrum using Equation (4) to determine the value of α, with $T_{\rm eq} = 2358$ K, log $g = 2.973$ (cgs) taken from Table 4 in Delrez et al. (2016) and the mean mass of atmospheric particles $\mu = 2.37$ assuming a hydrogen-dominated atmosphere. We derive $\alpha = -9.95^{+1.47}_{-1.49}$, which is much smaller than the predicted value $\alpha = -4$ if only the Rayleigh scattering effect is considered. This suggests that the Rayleigh scattering should not be the only cause for the observed steep slope in the transmission spectrum.

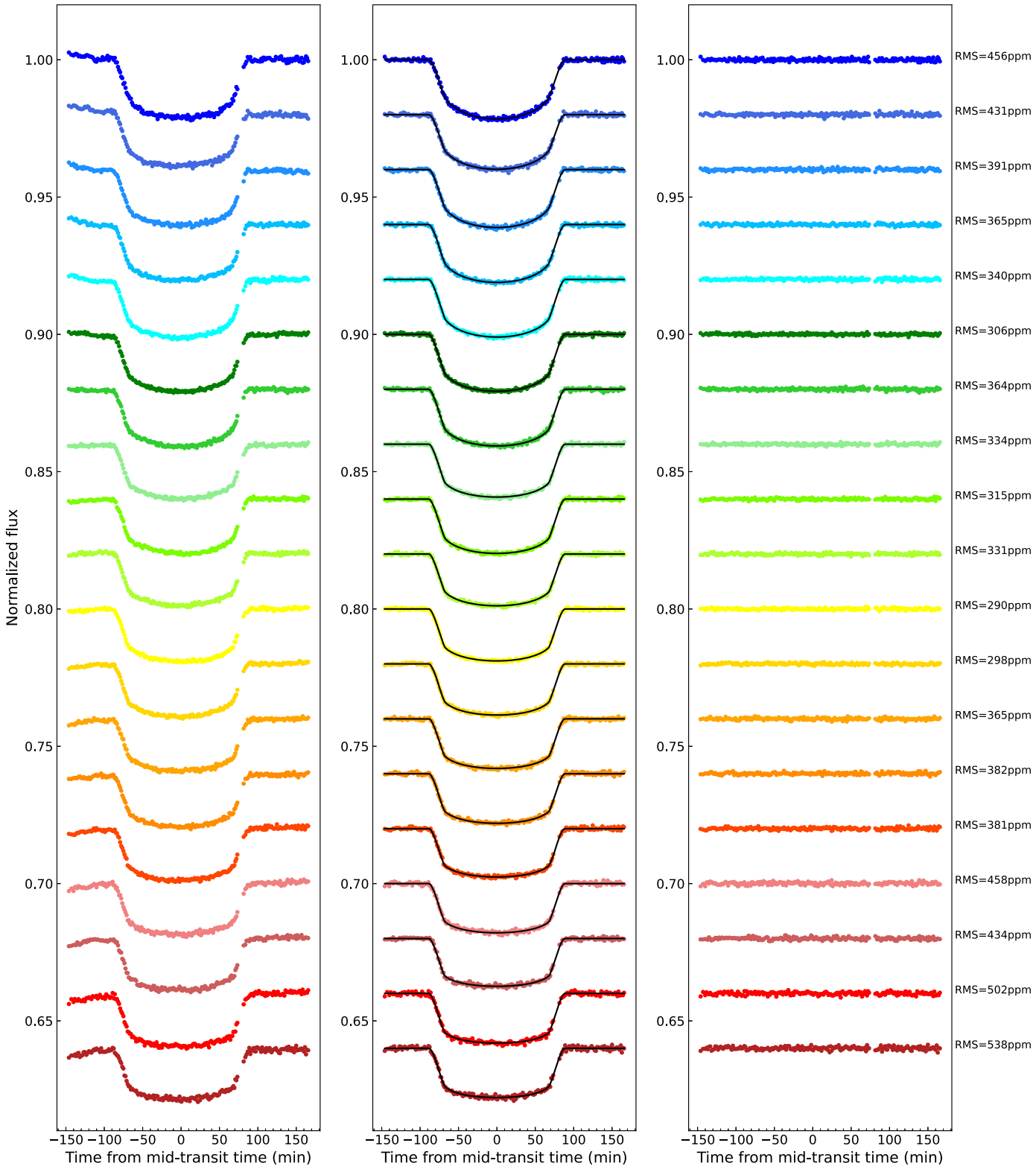

Figure 4. The 19 spectroscopic light curves obtained for Night 2. For distinction, a constant vertical offset and a different color was applied to each light curve. Left panel: the raw light curves with common-mode noise removed. Middle panel: the detrended light curves (colored dots) with the best-fit model curves (black lines). Right panel: the observation−model residuals.

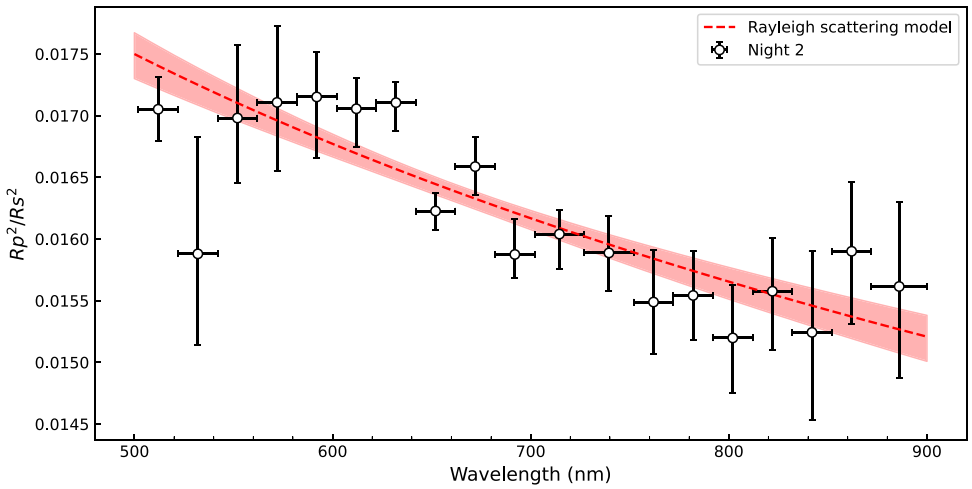

Figure 5. The SOAR/GHTS optical transmission spectrum obtained in this work with a Rayleigh scatting model; red shaded area is the 1σ confidence interval of the model.

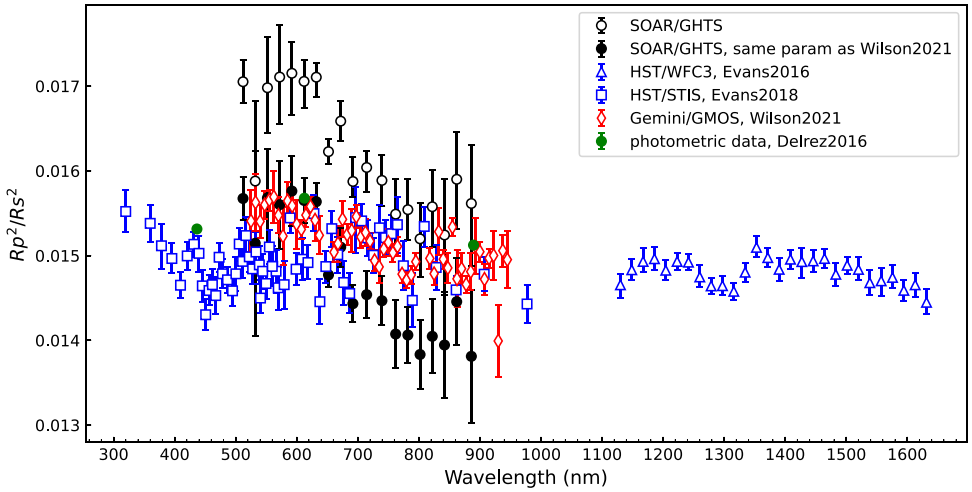

Figure 6. The optical and NIR transmission spectra obtained in this work and previous works.

4.3. Retrieval Analysis

To further evaluate the atmospheric composition and temperature structure of WASP-121b, we perform retrieval analysis on the derived transmission spectra. We use the `petitRADTRANS` package (Mollière et al. 2019) and the `PyMultiNest` package (Buchner et al. 2014) to generate a 1D model transmission spectrum and calculate the Bayesian evidence($\mathcal{Z}$). We adopt the two-point (2P) temperature-pressure ($T-P$) profile given by Brogi et al. (2014) and assume free chemistry to find the specific species causing the features in the transmission spectrum. For the 2P $T-P$ profile, the temperatures are constant at altitudes above the lower pressure point (T_1, P_1) or below the higher pressure point (T_2, P_2), and change linearly with $\log P$ between the two points. The parameters ($T_{1,2}$, $P_{1,2}$) are free parameters to be retrieved. Although a dozen atoms and molecules have been discovered in the atmosphere of WASP-121b, it is not realistic to retrieve all of them with our LR data obtained on a ground-based 4 m telescope. Therefore, we only take a few species including H_2O, VO, TiO, FeH, Na, Ca, Fe, Mg and V, which have relatively strong absorption in the optical and NIR. Molecular H_2 and He are treated as filling gases with atomic abundance ratios fixed to the solar values, and the Rayleigh scattering of H_2 and He is considered in the model spectra. The mass fractions of the other nine species are allowed to vary freely. In addition, the reference planet radius R_p is set as a free parameter, while the reference pressure P_0 is fixed to be 0.01 bar.

We perform in total three sets of retrieval analyses to explore the bulk composition of the atmosphere of WASP-121b. The first set is to find the most contributing species among H_2O, VO, TiO and FeH and determine their abundances, based on

Table 5
Statistics of All Retrieval Models

#	Model	OPT				ONIR			
		dof	χ^2_ν	ln $\mathcal{Z}$	Δ ln $\mathcal{Z}$	dof	χ^2_ν	ln $\mathcal{Z}$	Δ ln $\mathcal{Z}$
Only molecules									
A1	H_2O + VO					38	2.12	397.7	−16.5
A2	H_2O + VO + TiO					37	2.02	414.2	0
A3	H_2O + VO + FeH					37	2.18	397.1	−17.1
A4	H_2O + VO + TiO + FeH					36	2.03	413.0	−1.2
A2 + one atom									
B1	A2 + Ca					35	2.02	413.6	−1.5
B2	A2 + Fe					35	2.07	414.1	−1.0
B3	A2 + Mg					35	2.06	414.0	−1.1
B4	A2 + Na					35	1.99	413.4	−1.7
B5	A2 + V					35	1.55	415.1	0
B5 on the OPT data									
C1	B5	8	2.65	109.2	0				

the combination of our OPT data and the literature NIR transmission spectrum from Evans et al. (2016) (hereafter the ONIR data). We choose these four molecules because H_2O, VO, Fe I and Fe II have been firmly detected, while TiO has been tentatively detected (Evans et al. 2016, 2018; Sing et al. 2019; Gibson et al. 2020). We run four retrieval experiments to determine the best-fit of the model with different combinations of the four molecules (see Models A1-4 in Table 5). We find that Model 2 with H_2O, VO and TiO included matches best with the ONIR data, given its largest Bayesian evidence ln $\mathcal{Z}$ and the smallest reduced chi-square χ^2_ν. We note that this model is significantly better than the two models with TiO excluded, i.e., Models A1 and A3. It is also evident that adding FeH to the A2 model does not return better results, suggesting that the ONIR data do not support a significant presence of FeH in WASP-121b's atmosphere.

Next, we run another five models with each combination of the A2 model and one of the following atoms, Mg, Na, Ca, Fe or V, to explore the presence of them. The results are shown as Models B1 − 5 in Table 5. We find that B5 gives the best fits to the data set with χ^2_ν smaller than the A2 model, while the other models have smaller ln $\mathcal{Z}$ and larger χ^2_ν. This implies that WASP-121b's atmosphere may possess a large amount of the atom V. Finally, based on the B5 model, we perform retrieval analysis on the OPT data alone. This is to explore what we can infer if only data in the optical band are available. Unfortunately, the retrieval is not very robust given that the best-fit model returns a large χ^2_ν of 2.65.

The statistics of the retrievals mentioned above are summarized in Table 5. The best-fit models of the ONIR (the B5 model) and the OPT data (the C1 model) are shown in Figure 7, and the corresponding posterior distributions are listed in Table 6. It is noted that the derived planet radius from the OPT data is consistent with that from the ONIR data within 1σ, although a little bit larger. As illustrated in Figure A2, the presence of thermal inversion is favored by both retrievals, despite that the derived $T-P$ profiles are not very consistent with each other. Given that the optical transmission spectrum is from a ground-based telescope, while the NIR spectrum is from a space telescope, there might be an offset between these two data sets as noted previously by Murgas et al. (2020). Therefore, we add δ, the offset between the HST/WFC3 data and our SOAR data, as a free parameter for the ONIR retrievals.

The ONIR data yield a $\sim 14.2\sigma$, 6.6σ and 3.8σ detection of TiO, H_2O and VO, respectively. In addition, the atom V is detected with an abundance of $-3.77^{+1.03}_{-4.21}$, suggesting that the atom V may be present in WASP-121b's atmosphere. However, the ln $\mathcal{Z}$ value of the B5 model is only 0.9 larger than the A2

Table 6
The Posterior Distribution of All Retrieval Parameters From Best-fit Models of OPT and ONIR Data

Free Chemistry	Prior	Posterior of OPT	Posterior of ONIR
R_p (R_{jup})	$\mathcal{U}(1.6, 2.0)$	$1.803^{+0.022}_{-0.019}$	$1.774^{+0.020}_{-0.024}$
T_1 (K)	$\mathcal{U}(1500, 4000)$	3726^{+196}_{-311}	3626^{+252}_{-545}
log P_1(bar)	$\mathcal{U}(-6, -2)$	$-3.67^{+1.02}_{-1.27}$	$-4.08^{+1.03}_{-1.01}$
T_2 (K)	$\mathcal{U}(1500, 4000)$	2844^{+693}_{-750}	2004^{+1030}_{-351}
log P_2(bar)	$\mathcal{U}(-2, 3)$	$0.72^{+1.44}_{-1.66}$	$-0.77^{+2.18}_{-0.90}$
log P_{cloud}(bar)	$\mathcal{U}(-6, 3)$	$0.54^{+1.52}_{-1.61}$	$-1.39^{+0.77}_{-1.55}$
log X_{H_2O}	$\mathcal{U}(-10, 0)$	$-6.30^{+2.59}_{-2.29}$	$-4.13^{+0.63}_{-0.46}$
log X_V	$\mathcal{U}(-10, 0)$	$-1.61^{+0.46}_{-0.67}$	$-3.77^{+1.03}_{-4.21}$
log X_{TiO}	$\mathcal{U}(-10, 0)$	$-7.54^{+0.60}_{-0.74}$	$-5.95^{+0.47}_{-0.42}$
log X_{VO}	$\mathcal{U}(-10, 0)$	$-8.89^{+0.82}_{-0.68}$	$-6.72^{+0.51}_{-1.79}$
δ (ppm)	$\mathcal{U}(-10{,}000, 10{,}000)$	⋯	-241^{+264}_{-422}
ln $\mathcal{Z}$	⋯	109.2	415.1
χ^2_ν	⋯	2.65	1.55

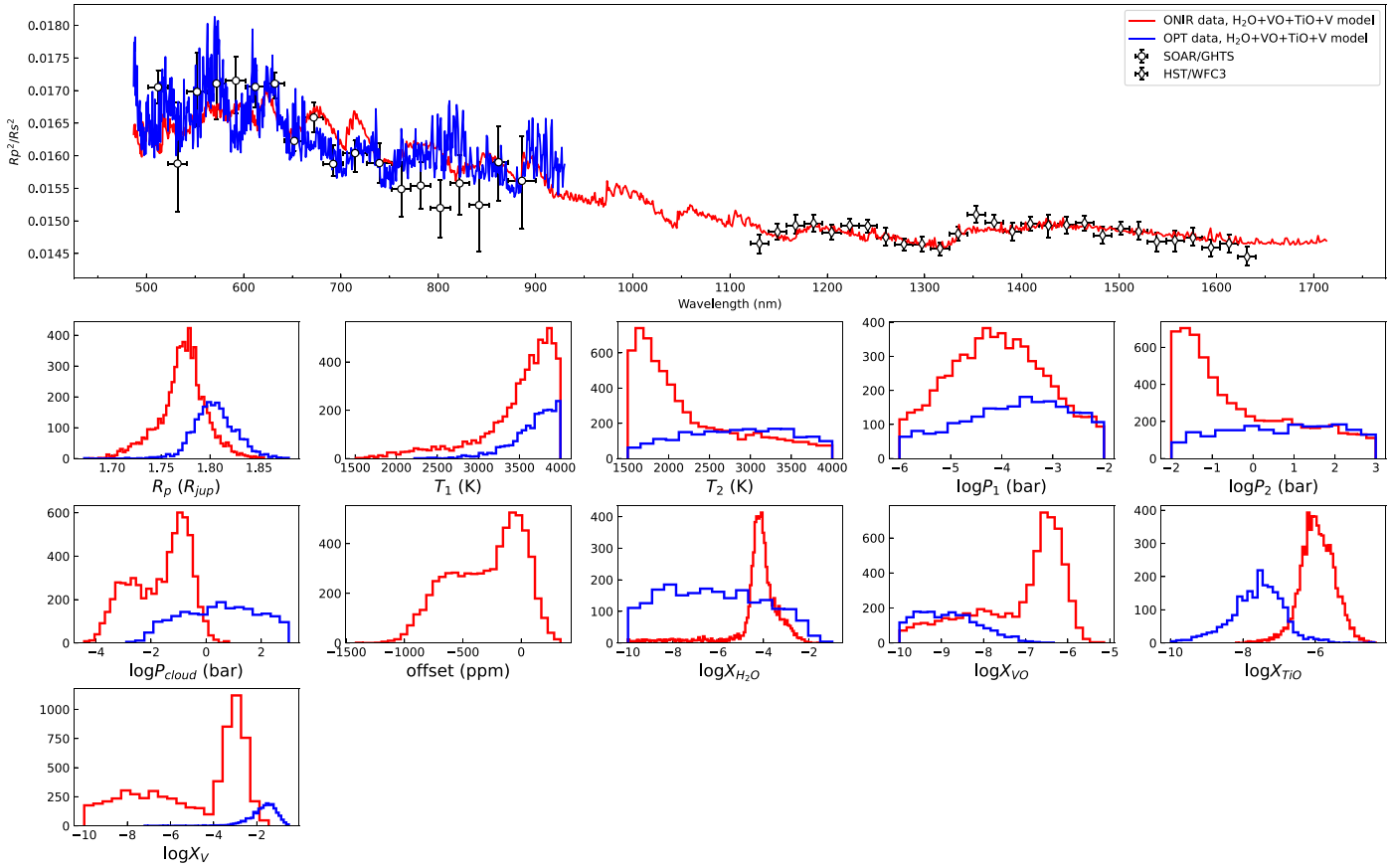

Figure 7. The OPT and ONIR transmission spectra of WASP-121b with best-fit models overplotted. Black open circles with error bars: the SOAR optical transmission spectrum derived in this work. Black open diamonds with error bars: the HST/WFC3 NIR transmission spectrum from Evans et al. (2016). The blue and red solid lines are the best-fit retrieval models for OPT and ONIR data, respectively.

model, and there is a long tail extending to lower abundance in the posterior distribution plot in Figure 7. Therefore, we can only claim a tentative detection of V with the abundance upper limit as <-2.74 in this work. For comparison, the retrieval analysis on the OPT data is not ideal, with only TiO and VO reasonably well constrained with $\log X_{\rm TiO} = -7.54^{+0.60}_{-0.74}$ and $\log X_{\rm VO} = -8.89^{+0.82}_{-0.68}$, respectively. However, the derived V abundance is too high to be real, which may be the cause for the relatively smaller abundances of TiO and VO with respect to those from the ONIR data. We suggest that the worse precision of the optical transmission spectrum hinders the accurate constraint of some species and $T-P$ profile. To conclude, the B5 model yields the best result. The retrieval models and the posterior distribution plots of the A and B series models are shown in Figures A3 and A4, respectively.

5. Discussion

5.1. Stellar Activity

As mentioned in Pont et al. (2008), McCullough et al. (2014), Rackham et al. (2017, 2018), stellar activity such as unocculted spots and faculae may cause variation in a transmission spectrum. As for WASP-121, several previous works discussed the impact of stellar activity on the associated transmission spectrum. The discovery paper of Delrez et al. (2016) monitored the out-of-eclipse photometric variability from 27 non-consecutive nights between 2014 October 25 and December 8 using TRAPPIST. They found WASP-121 to be very quiet with standard deviation of 1.3 mmag in their $V-$band light curves. Evans et al. (2016) attributed the different radii measured at optical and NIR wavelengths to unocculted spots, and they claimed that the spot coverage should be $\sim$7% of the visible stellar disk. They further used the Celestron 14 inch (C14) Automated Imaging Telescope (AIT) to monitor the host star activity in two campaigns (2017 January 27 to April 23 and 2018 February 22 to April 8) (Evans et al. 2018, Appendix B.3), and concluded that WASP-121 had been photometrically stable over multi-week periods at the $\sim$5–1 mmag level. Further works of Evans et al. (2018) and Wilson et al. (2021) also suggested the stellar activity should be negligible, and it should not be responsible for the variation in transmission spectrum.

Our observation was taken during the second monitoring program of Evans et al. (2018). As demonstrated in their Figure B.3, the peak-to-valley amplitudes at that time were $\sim 0.00320 \pm 0.00096$ mag, while the period of host star activity was 6.66 days, ~80 times larger than our relevant timescale of ~hours. Therefore, we believe that the obtained transmission spectrum of WASP-121b should be untouched by the activity of its host star.

5.2. Composition of the Atmosphere

Several previous works studied the atmospheric composition of WASP-121b with LR and HR transmission spectra. Many molecules, atoms and ions have been detected or confirmed in the atmosphere of WASP-121b (e.g., H_2O, Ca I, Ca II, Cr, Fe I, Fe II, K, Li, Mg, Na, Ni, Sc II, V, TiO and VO). However, the existence of TiO and VO is still controversial. In E16, the authors suggested the deeper transit depth in the optical passband to be evidence for the presence of TiO and VO. This was further supported in Evans et al. (2017) by the discovery of the thermal inversion layer on the dayside from their NIR thermal spectrum. However, several theoretical research efforts indicated TiO/VO may not be the only absorber to induce thermal inversion. Some other metal-rich species (Fe, Mg, SiO, AlO, CaO, NaH and MgH) could also cause thermal inversion (Lothringer et al. 2018; Gandhi et al. 2020). In addition, mechanical greenhouse effects may heat the atmosphere or suppress cooling and induce thermal inversion (Youdin & Mitchell 2010). Further optical transmission spectroscopy observation by HST/STIS only obtained a detection of VO and an upper limit for TiO (E18). High-resolution transmission spectra of WASP-121b (Bourrier et al. 2020; Cabot et al. 2020; Ben-Yami et al. 2020; Gibson et al. 2020; Hoeijmakers et al. 2020; Borsa et al. 2021; Merritt et al. 2021; Gibson et al. 2022) have detected and confirmed Fe and V, but the existence of titanium and its oxide still remains controversial.

E18 reported the detection of VO and TiO with abundances of $-6.6^{+0.2}_{-0.3}$ and <-7.9, respectively. W21 obtained the mass fractions of VO and TiO as $\log X_{\rm VO} = -10.74^{+0.49}_{-0.56}$ and $\log X_{\rm TiO} = -9.98^{+0.38}_{-0.65}$, respectively. These two works are obviously not consistent. Actually, the optical transmission spectra obtained in these two works differ from each other (see colored dots in Figure 6). E18 ran a series of robustness tests, including the treatment of LD coefficients and the additional parameters of GP inputs. They found that the measured transmission spectrum obtained by different instruments (G430L and G750L gratings) could not be explained by one self-consistent model. Later, W21 reported the discrepancy in the optical transmission spectrum, and pointed out that the transmission spectrum may vary with time. W21 and references therein (Parmentier et al. 2013; Komacek & Showman 2020) pointed out that the temperature fluctuations might result in significant spatial and temporal variations in atmospheric constituents, and could lead to measurable variations in the transmission spectrum, with a predictable variation period of 50–100 days. The E18 observations were taken in 2016 October and November, while the W21 data were obtained in 2017 January, and our observations were carried out in 2018 March. These data sets have a long time separation with 60 and 420 days, which is consistent with the variation timescale mentioned above. Therefore, the possibility of temporal variation of transmission spectra cannot be rejected.

From our ONIR retrieval analysis, we obtain clear detection of TiO with $\log X_{\rm TiO} = -5.95^{+0.47}_{-0.42}$, which is much higher than the upper limit from E18 and the abundance from W21. As for VO, its mass fraction is estimated to be $-6.72^{+0.51}_{-1.79}$ dex in this work, consistent with that from E18 with $\sim 2.7\sigma$ confidence, and is significantly larger than that from W21. These abundance discrepancies confirm that the physical and chemical conditions in the terminator region of WASP-121b may indeed change with time. In addition, we detect a strong water absorption with the abundance of $\log X_{\rm H_2O} = -4.13^{+0.63}_{-0.46}$, which is between the abundance from Evans et al. (2018) ($-2.2^{+0.3}_{-0.3}$) and Wilson et al. (2021) ($-5.05^{+0.19}_{-0.18}$). The discrepancy of H_2O abundance may come from the retrieval model assumption and the difference in optical spectra, due to E18, W21 and this work using the same HST/WFC3 transmission spectrum from Evans et al. (2016).

Interestingly, as shown in the posterior distribution in Figure 7, there is actually another peak of VO in the lower abundance regime at about -9 dex, consistent with that from W21. This bimodal distribution is also visible in the distribution plots and corner plots of the cloud pressure, the fraction of V and δ (the offset between the HST data and the SOAR data). We find that these parameters may be coupled with each other, which might be why there are two possible solutions that can be deduced from the obtained transmission spectra. For the case that δ is close to zero, large amounts of V and VO are required to enhance the optical opacity to balance between the optical and the NIR transmission spectra. For the case with negative δ adopted, the HST transmission spectrum will be raised up to match better with the optical transmission spectrum, resulting in much smaller requirements for the abundances of V and VO. It is interesting to note that both E18 and W21 yielded lower TiO and/or VO abundances, which might be due to adopting a constant $a/R_\star$ and b (or i) in the optical and NIR bands for their light curve fittings. As $R_{\rm p}/R_\star$ is highly dependent on $a/R_\star$ and b, using the same $a/R_\star$ and b would result in aligning $R_{\rm p}/R_\star$ values in the optical and NIR bands. This aligning is effectively similar to applying an offset to the NIR transmission spectrum to match the optical one, just like the second case discussed above.

6. Conclusion

In this work, we report on a study of the UHJ WASP-121b based on our ground-based 4 m telescope SOAR/GHTS optical transit observation and literature HST NIR transmission spectra. The SOAR observations were taken on the nights of 2018 February 7 and March 1, but the first night only covered a partial transit due to weather loss. As a result, only data taken in the second night were employed in this study. By dividing the stellar spectra into 19 passbands, we extracted 19 spectroscopic transit light curves and fit them using the GP method. Then we derived transit depths in 19 spectral bins, i.e., the transmission spectrum of WASP-121b. The stellar activity of the host star is weak with variation of $0.003\,20 \pm 0.00096$ mag over a period of $\sim$6.6 days from the simultaneous photometric monitoring program by Evans et al. (2018), and thus should not produce an unignorable imprint on our obtained transmission spectrum with a timescale of $\sim$h.

The derived optical transmission spectrum shows an increased slope toward blue wavelength with a slope $\alpha = -9.95^{+1.47}_{-1.49}$, much smaller than the hydrogen-dominated Rayleigh scattering ($\alpha = -4$), which could not be explained by Rayleigh scattering alone. There are notable differences between our spectrum and those in the literature from Evans et al. (2018), Wilson et al. (2021), which imply that the atmosphere of WASP-121b may experience temporal variation. Note that our data analysis procedures passed our validation experiment, by the small offset $\sim 472 \pm 286 \pm 25$ ppm between the GMOS transmission spectra derived by us from the 1D spectra provided by Dr. Jamie Wilson and Dr. Neale Gibson via private communication with those from Wilson et al. (2021). This small difference is caused by the different setting in orbital parameters during the light curve analysis.

Retrieval analyses are performed on the optical data and the combination of the optical data and literature HST/WFC3 NIR data, to evaluate the composition and temperature structure of WASP-121b. Both analyses support the presence of a thermal inversion layer on the day-side atmosphere, with turn-over point parameters consistent with each other within their quoted uncertainties. The best model is the one obtained on the combined data set considering TiO, VO, H_2O and atom V, which yields a clear detection of TiO with $\log X_{\rm TiO} = -5.95^{+0.47}_{-0.42}$, much higher than those from E18 and W21. VO is also detected with the median $\log X_{\rm VO} = -6.72$ plus another peak at ~ -9. While the median value is consistent with that from E18, the secondary peak is in line with that from W21. Although other species like SiO and mechanical greenhouse effects can also induce thermal inversion, the transmission data collected in this work favor the presence of TiO in WASP-121b, as discussed in Section 5.2.

We argue that some parameters, particularly the NIR-to-OPT offset δ, the cloud deck pressure, and abundances of VO and V, may be coupled, as illustrated by the double clumps seen in the corner distribution of the above-mentioned parameters in Figure A6. If fixing δ to zero, more V and VO are required to enhance the opacity in the optical to account for the discrepancy between the optical and NIR transmission spectra. On the other hand, setting a negative δ, which raises up the HST transmission spectra, results in much smaller requirements for the contribution from V and VO. Therefore, we caution that putting δ into retrieval may induce further uncertainties.

To summarize, the discrepancies seen in the optical transmission spectra and the determined abundances of VO, TiO and H_2O between this work and those from literature provide direct evidence of the variation of WASP-121b's atmosphere, as suggested by Wilson et al. (2021). According to their work and the references therein, the $T-P$ profile of the WASP-121b atmosphere may lie near the condensation curves of a number of species, which may result in significant temporal variations in the atmospheric components. Therefore, we strongly recommend that multi-epoch LR and HR transit observations should be conducted for WASP-121b to study the temporal variation in its transmission spectrum.

Acknowledgments

We thank the anonymous reviewer for their constructive comments. We also thank Dr. Jamie Wilson and Dr. Neale P. Gibson for providing Gemini/GMOS data. This research is supported by the National Key R&D Program of China Nos. 2019YFA0405102 and 2019YFA0405502, and the National Natural Science Foundation of China (NSFC, Grant Nos. 42075123, 62127901, 11988101, 42005098, and 12073044). This work is also supported by the China Manned Space Project with No. CMS-CSST-2021-B12. M.Z. and Q.-L. O.-Y are supported by the Chinese Academy of Sciences (CAS), through a grant to the CAS South America Center for Astronomy (CASSACA) in Santiago, Chile.

This work is based on observations obtained at the Southern Astrophysical Research (SOAR) Telescope, which is a joint project of the Ministério da Ciência, Tecnologia e Inovações (MCTI/LNA) do Brasil, the US National Science Foundation's NOIRLab, the University of North Carolina at Chapel Hill (UNC), and Michigan State University (MSU).

Appendix
Additional Figures

In this appendix we provide some supplementary figures for this manuscript (Figures A1–A6).

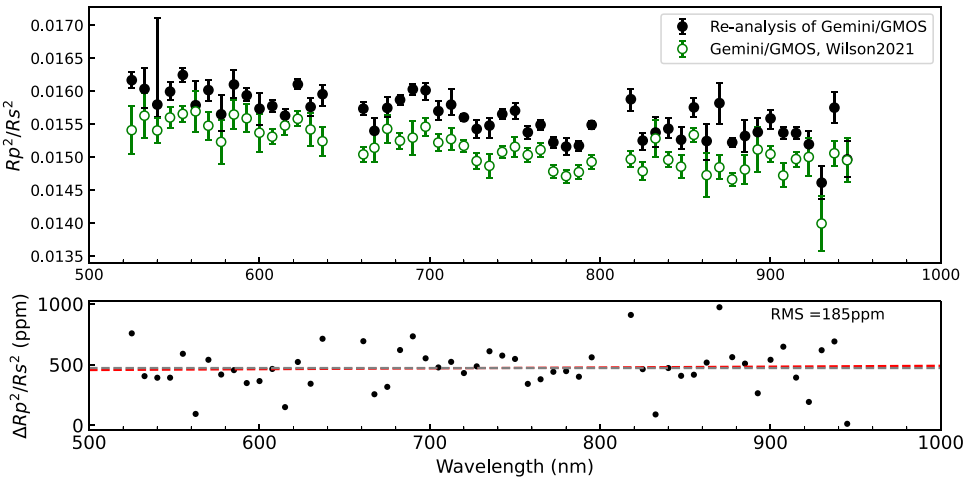

Figure A1. Top: the optical transmission spectrum of WASP-121b obtained by Gemini/GMOS. The black circular dots with error bars are the Gemini/GMOS transmission spectrum re-analyzed by us, while the green circular dots are the transmission spectrum published in Wilson et al. (2021). Both results are very consistent. Bottom: the $\Delta R_p^2/R_s^2$ of the two transmission spectra. The dashed gray line is the mean value of $\Delta R_p^2/R_s^2 = 472$ ppm, and the dashed red line is a simple linear polynomial function to fit these $\Delta R_p^2/R_s^2$, which is very close to the mean value.

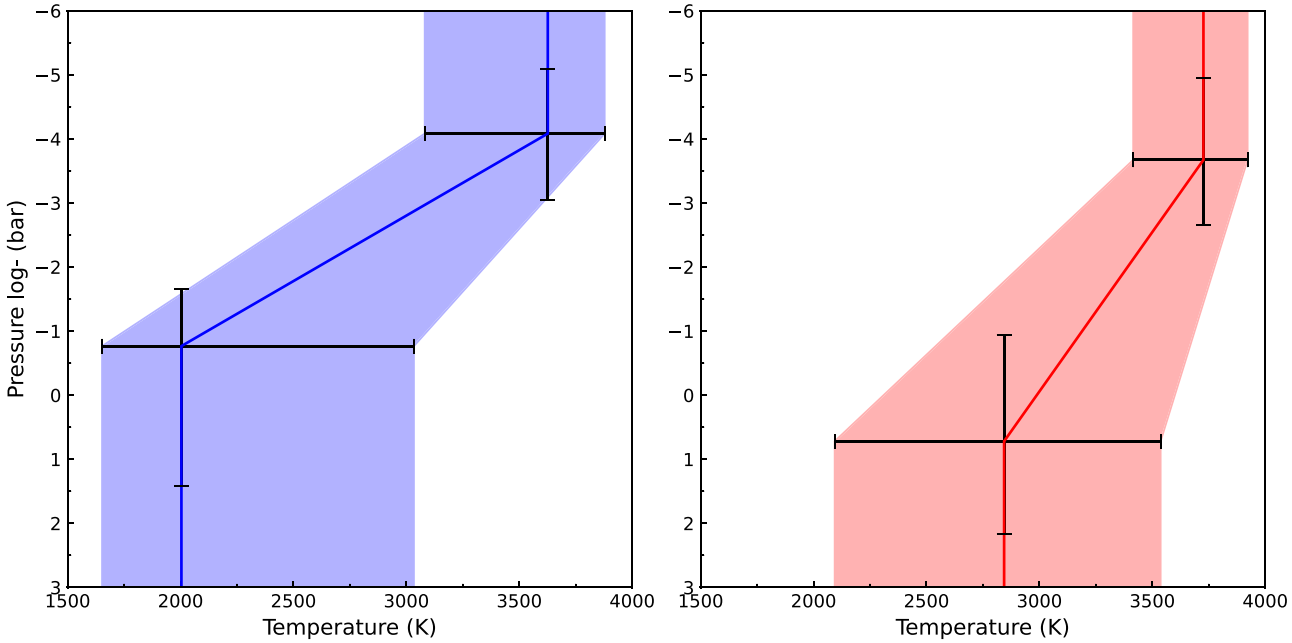

Figure A2. Left: the $T - P$ profile retrieved from OPT data and the 1σ confidence interval. Right: the $T - P$ profile retrieved from ONIR data and the 1σ confidence interval.

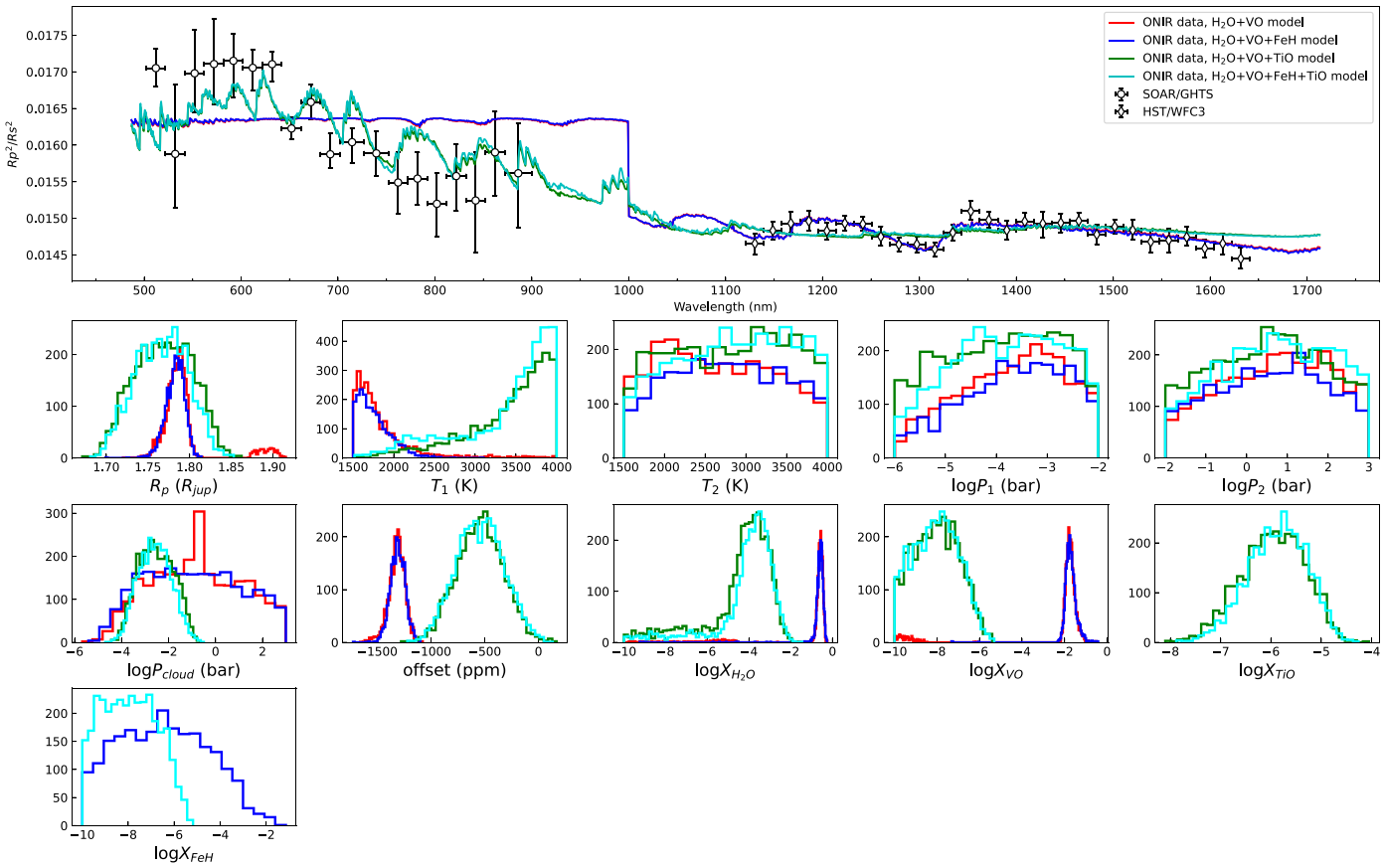

Figure A3. Same as Figure 7, the retrieval models and posterior distributions of the first step in retrieval.

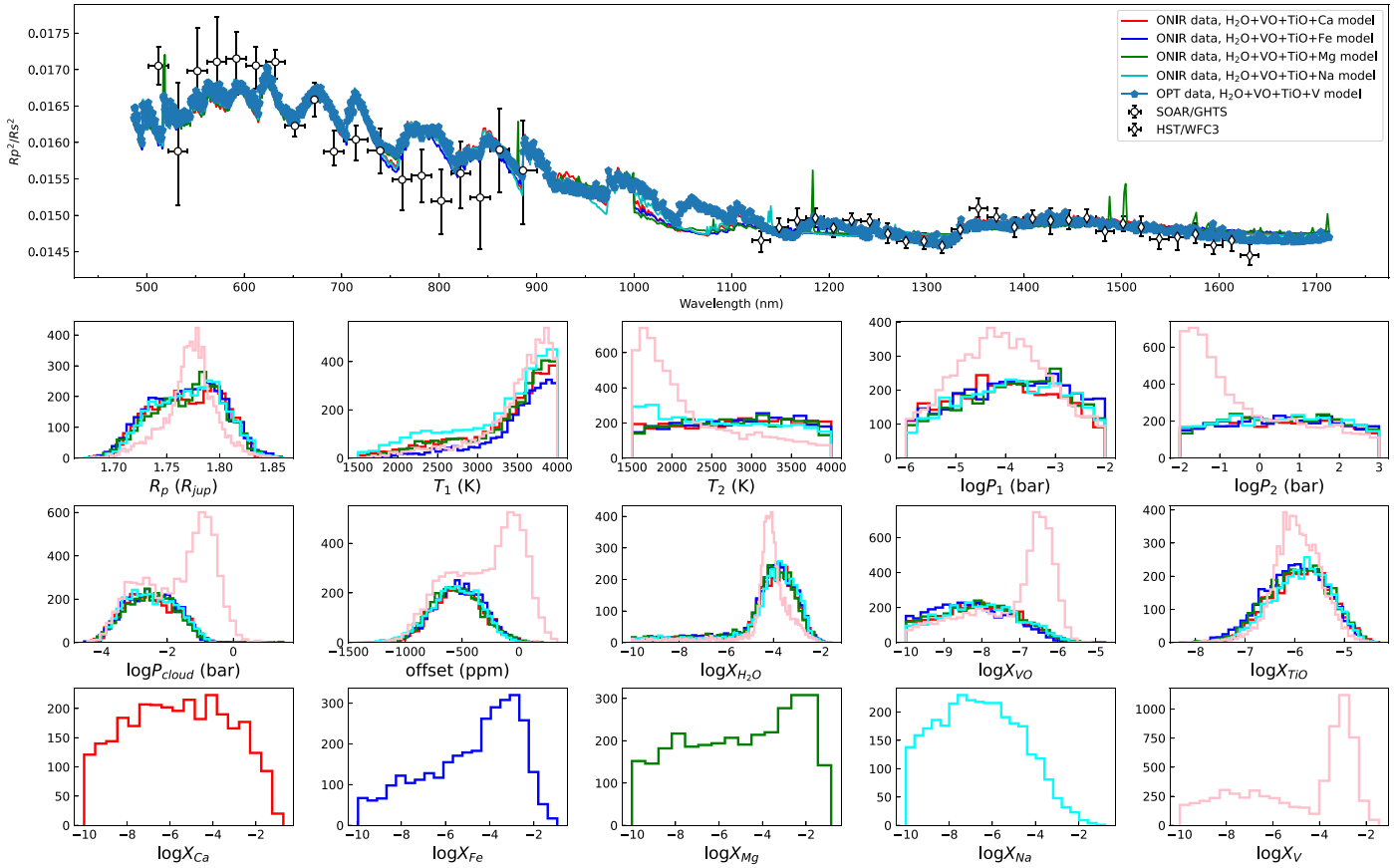

Figure A4. Same as Figure 7, the retrieval models and posterior distributions of the second step in retrieval.

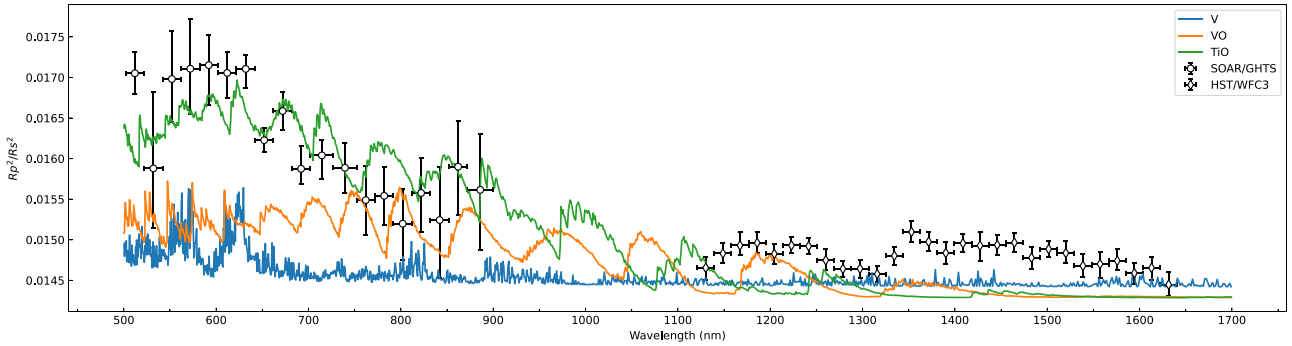

Figure A5. The OPT and ONIR transmission spectrum of WASP-121b with the contribution of V, VO and TiO.

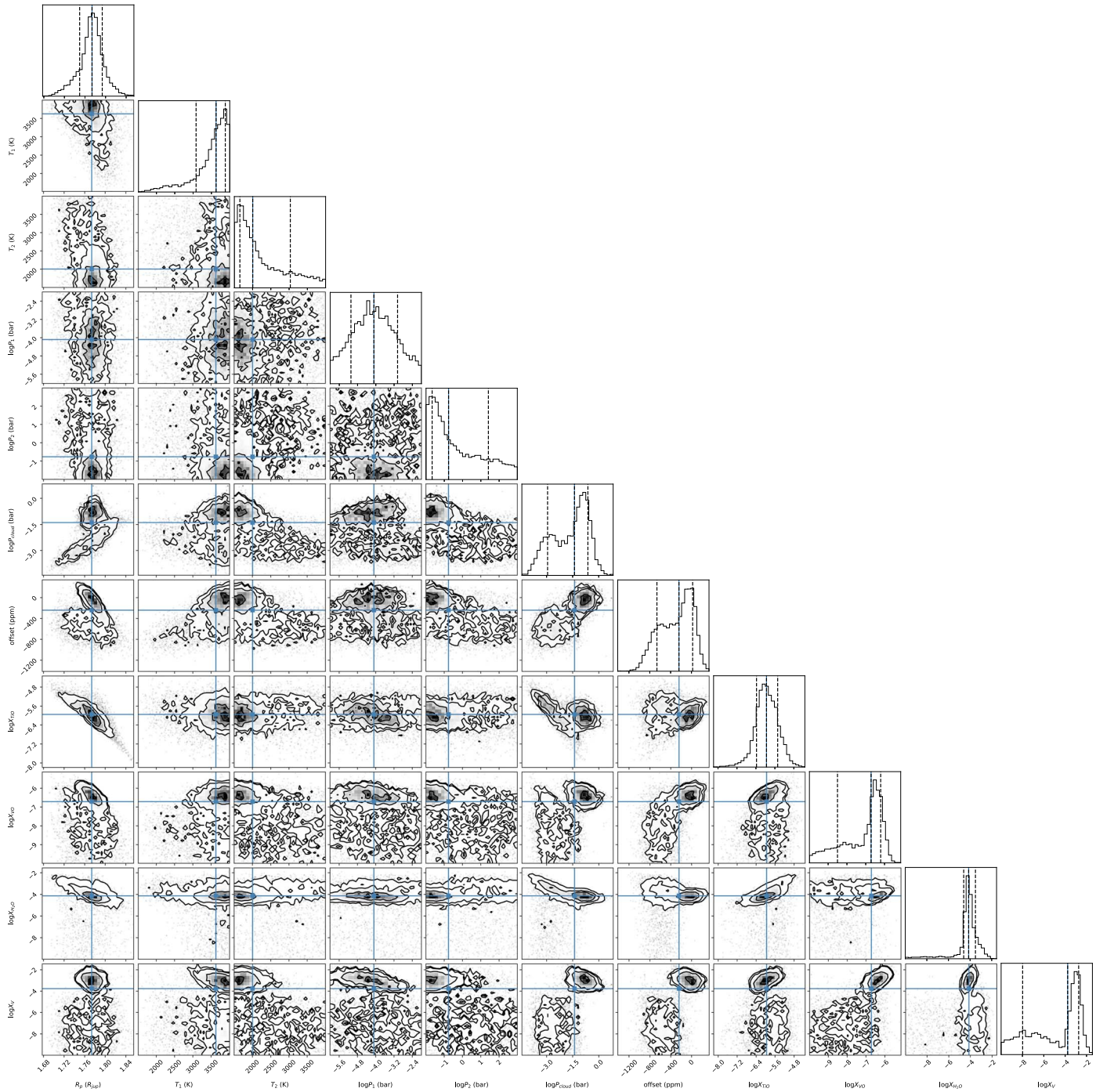

Figure A6. The posterior distribution corner plot of the B5 model in Table 5.

ORCID iDs

Wei Wang https://orcid.org/0000-0002-9702-4441
Fei Zhao https://orcid.org/0000-0003-4276-1767

References

Alderson, L., Kirk, J., López-Morales, M., et al. 2020, MNRAS, 497, 5182
Alexoudi, X., Mallonn, M., Keles, E., et al. 2020, A&A, 640, A134
Alexoudi, X., Mallonn, M., von Essen, C., et al. 2018, A&A, 620, A142
Ambikasaran, S., Foreman-Mackey, D., Greengard, L., et al. 2015, ITPAM, 38, 252
Beaulieu, J. P., Kipping, D. M., Batista, V., et al. 2010, MNRAS, 409, 963
Ben-Yami, M., Madhusudhan, N., Cabot, S. H. C., et al. 2020, ApJL, 897, L5
Borsa, F., Allart, R., Casasayas-Barris, N., et al. 2021, A&A, 645, A24
Bourrier, V., Ehrenreich, D., Lendl, M., et al. 2020, A&A, 635, A205
Brogi, M., de Kok, R. J., Birkby, J. L., et al. 2014, A&A, 565, A124
Buchner, J., Georgakakis, A., Nandra, K., et al. 2014, A&A, 564, A125
Cabot, S. H. C., Madhusudhan, N., Welbanks, L., Piette, A., & Gandhi, S. 2020, MNRAS, 494, 363
Casasayas-Barris, N., Palle, E., Nowak, G., et al. 2017, A&A, 608, A135
Charbonneau, D., Brown, T. M., Latham, D. W., & Mayor, M. 2000, ApJL, 529, L45
Chen, G., Pallé, E., Parviainen, H., et al. 2021b, MNRAS, 500, 5420
Chen, G., Pallé, E., Parviainen, H., Murgas, F., & Yan, F. 2021a, ApJL, 913, L16
Chen, G., Pallé, E., Welbanks, L., et al. 2018, A&A, 616, A145
Clemens, J. C., Crain, J. A., & Anderson, R. 2004, Proc. SPIE, 5492, 331
Deibert, E. K., de Mooij, E. J. W., Jayawardhana, R., et al. 2021, ApJL, 919, L15
Delrez, L., Santerne, A., Almenara, J. M., et al. 2016, MNRAS, 458, 4025
Deming, D., Wilkins, A., McCullough, P., et al. 2013, ApJ, 774, 95
Eastman, J., Siverd, R., & Gaudi, B. S. 2010, PASP, 122, 935
Ehrenreich, D., Lovis, C., Allart, R., et al. 2020, Natur, 580, 597
Evans, T. M., Aigrain, S., Gibson, N., et al. 2015, MNRAS, 451, 680
Evans, T. M., Sing, D. K., Goyal, J. M., et al. 2018, AJ, 156, 283
Evans, T. M., Sing, D. K., Kataria, T., et al. 2017, Natur, 548, 58
Evans, T. M., Sing, D. K., Wakeford, H. R., et al. 2016, ApJL, 822, L4
Foreman-Mackey, D., Hogg, D. W., Lang, D., & Goodman, J. 2013, PASP, 125, 306
Gandhi, S., Madhusudhan, N., & Mandell, A. 2020, AJ, 159, 232
Giacobbe, P., Brogi, M., Gandhi, S., et al. 2021, Natur, 592, 205
Gibson, N. P., Aigrain, S., Barstow, J. K., et al. 2013, MNRAS, 428, 3680
Gibson, N. P., Aigrain, S., Roberts, S., et al. 2012, MNRAS, 419, 2683
Gibson, N. P., Merritt, S., Nugroho, S. K., et al. 2020, MNRAS, 493, 2215
Gibson, N. P., Nugroho, S. K., Lothringer, J., Maguire, C., & Sing, D. K. 2022, MNRAS, 512, 4618
Hoeijmakers, H. J., Ehrenreich, D., Heng, K., et al. 2018, Natur, 560, 453
Hoeijmakers, H. J., Seidel, J. V., Pino, L., et al. 2020, A&A, 641, A123
Høg, E., Fabricius, C., Makarov, V. V., et al. 2000, A&A, 355, L27
Horne, K. 1986, PASP, 98, 609
Husser, T.-O., Wende-von Berg, S., Dreizler, S., et al. 2013, A&A, 553, A6
Kirk, J., López-Morales, M., Wheatley, P. J., et al. 2019, AJ, 158, 144
Kirk, J., Rackham, B. V., MacDonald, R. J., et al. 2021, AJ, 162, 34
Kirk, J., Wheatley, P. J., Louden, T., et al. 2016, MNRAS, 463, 2922
Kirk, J., Wheatley, P. J., Louden, T., et al. 2017, MNRAS, 468, 3907
Kirk, J., Wheatley, P. J., Louden, T., et al. 2018, MNRAS, 474, 876
Komacek, T. D., & Showman, A. P. 2020, ApJ, 888, 2
Kreidberg, L. 2015, PASP, 127, 1161
Lecavelier Des Etangs, A., Pont, F., Vidal-Madjar, A., & Sing, D. 2008, A&A, 481, L83
Lothringer, J. D., Barman, T., & Koskinen, T. 2018, ApJ, 866, 27
Madhusudhan, N. 2019, ARA&A, 57, 617
Maguire, C., Gibson, N. P., Nugroho, S. K., et al. 2023, MNRAS, 519, 1030
Mandel, K., & Agol, E. 2002, ApJL, 580, L171
McCullough, P. R., Crouzet, N., Deming, D., & Madhusudhan, N. 2014, ApJ, 791, 55
Merritt, S. R., Gibson, N. P., Nugroho, S. K., et al. 2021, MNRAS, 506, 3853
Mikal-Evans, T., Sing, D. K., Barstow, J. K., et al. 2022, NatAs, 6, 471
Mikal-Evans, T., Sing, D. K., Goyal, J. M., et al. 2019, MNRAS, 488, 2222
Mikal-Evans, T., Sing, D. K., Kataria, T., et al. 2020, MNRAS, 496, 1638
Mollière, P., Wardenier, J. P., van Boekel, R., et al. 2019, A&A, 627, A67
Murgas, F., Chen, G., Nortmann, L., Palle, E., & Nowak, G. 2020, A&A, 641, A158
Ouyang, Q., Wang, W., Zhai, M., et al. 2023, arXiv:2303.13202
Parmentier, V., Showman, A. P., & Lian, Y. 2013, A&A, 558, A91
Parviainen, H., & Aigrain, S. 2015, MNRAS, 453, 3821
Pont, F., Knutson, H., Gilliland, R. L., Moutou, C., & Charbonneau, D. 2008, MNRAS, 385, 109
Pych, W. 2004, PASP, 116, 148
Rackham, B., Espinoza, N., Apai, D., et al. 2017, ApJ, 834, 151
Rackham, B. V., Apai, D., & Giampapa, M. S. 2018, ApJ, 853, 122
Rasmussen, C. E., & Williams, C. K. I. 2006, Gaussian Processes for Machine Learning (Cambridge, MA: MIT Press)
Schwarz, G. 1978, AnSta, 6, 461
Sedaghati, E., Boffin, H. M. J., MacDonald, R. J., et al. 2017, Natur, 549, 238
Sing, D. K., Lavvas, P., Ballester, G. E., et al. 2019, AJ, 158, 91
Tody, D. 1986, Proc. SPIE, 627, 733
Tody, D. 1993, in ASP Conf. Ser. 52, Astronomical Data Analysis Software and Systems II, ed. R. J. Hanisch, R. J. V. Brissenden, & J. Barnes (San Francisco, CA: ASP), 173
Wilson, J., Gibson, N. P., Lothringer, J. D., et al. 2021, MNRAS, 503, 4787
Yan, D., Guo, J., Huang, C., & Xing, L. 2021, ApJL, 907, L47
Youdin, A. N., & Mitchell, J. L. 2010, ApJ, 721, 1113